Interplay of Nanoscale Strain and Smectic Susceptibility in Kagome Superconductors

Yidi Wang,[1,*,‡] Hong Li,[1,*,§] Siyu Cheng,[1] He Zhao,[1,∥] Brenden R. Ortiz,[2,3] Andrea Capa Salinas,[3]
Stephen D. Wilson,[3] Ziqiang Wang,[1] and Ilija Zeljkovic[1,†]

[1] *Department of Physics, Boston College, Chestnut Hill, Massachusetts 02467, USA*
[2] *Materials Science and Technology Division, Oak Ridge National Laboratory,*
Oak Ridge, Tennessee 37831, USA
[3] *Materials Department, University of California Santa Barbara, Santa Barbara, California 93106, USA*

(Received 18 November 2024; revised 24 March 2025; accepted 11 April 2025; published 30 May 2025)

Exotic quantum solids can host electronic states that spontaneously break rotational symmetry of the electronic structure, such as electronic nematic phases and unidirectional charge density waves (CDWs). When electrons couple to the lattice, uniaxial strain can be used to anchor and control this electronic directionality. Here, we reveal an unusual impact of strain on unidirectional "smectic" CDW orders in kagome superconductors AV_3Sb_5 using spectroscopic-imaging scanning tunneling microscopy. We discover local decoupling between the smectic electronic director axis and the direction of anisotropic strain. While the two can generally be aligned along the same direction in regions of a small CDW gap, the tendency for alignment decreases in regions where the CDW gap is the largest. This feature, in turn, suggests nanoscale variations in smectic susceptibility, which we attribute to a combination of local strain and electron correlation strength. Overall, we observe an unusually high decoupling rate between the smectic electronic director of the three-state Potts order and anisotropic strain, revealing weak smectoelastic coupling in the CDW phase of kagome superconductors. This finding is phenomenologically different from the extensively studied nematoelastic coupling in the Ising nematic phase of Ising nematic phase of Fe-based superconductor bulk single crystals, providing a contrasting picture of how strain can control electronic unidirectionality in different families of quantum materials.

DOI: 10.1103/PhysRevX.15.021074 Subject Areas: Condensed Matter Physics

I. INTRODUCTION

In quantum materials with substantial correlation effects, electrons often form phases with reduced symmetry groups compared to those of the underlying lattice structure, including, for example, electronic nematic and smectic phases in high-temperature superconductors and Moiré systems [1–3], where certain in-plane mirror symmetries are broken, resulting in an electronic band structure that is different along nominally equivalent lattice directions. Another canonical example is the stripelike charge ordering in cuprate high-temperature superconductors, where both rotational and translational symmetry are simultaneously broken to form a "smectic" electronic phase [1].

The family of AV_3Sb_5 (A stands for K, Cs, or Rb) kagome superconductors recently emerged as a rich playground to study symmetry-broken electronic phenomena [4–31]. In particular, the $2a_0 \times 2a_0$ charge-density-wave (CDW) phase (onset temperature $T^* \sim 80$–100 K [32–34]) that appears to break time-reversal symmetry [4,6,17,22] has attracted tremendous attention for potential realization of exotic orbital loop currents [11,35–37]. This phase also breaks the sixfold rotational symmetry of the lattice [4–6,24,38], with a single in-plane reflection symmetry that remains, suggesting a unidirectional nature of the phase. We refer to this phase as a "smectic" phase since it breaks both rotational and translation symmetries of the lattice, which is different from a nematic phase that only breaks rotational symmetry [39]. An additional $4a_0$ stripe order forms below 50–60 K [30]. While still under debate, the origin of the $2a_0 \times 2a_0$ order is generally attributed to a combination of electron-phonon coupling and nesting of van Hove singularities at M points [40]. The origin of the

---

[*] These authors contributed equally to this work.

[†] Contact author: ilija.zeljkovic@bc.edu

[‡] Present address: Department of Physics, Harvard University, Cambridge, MA 02138, USA.

[§] Present address: Department of Condensed Matter Physics & Material Science, Brookhaven National Laboratory, Upton, NY 11973, USA.

[∥] Present address: Department of Physics, Florida State University, Tallahassee, Florida 32306, USA.

$4a_0$ order is hypothesized to be due to nesting between small Fermi pockets, induced by band folding as the system goes through the $2a_0 \times 2a_0$ phase transition [31,37].

In materials where electrons strongly couple to the lattice, uniaxial strain can be a powerful tool for controlling the directionality of symmetry-breaking phenomena [41–48]—for instance, by anchoring the nematic axis [41–43,49,50]. These experiments typically rely on either applying a hydrostatic pressure that simultaneously compresses all crystalline directions or exerting in-plane strain, which in turn allows the out-of-plane lattice parameter to respond such that volume is approximately conserved. The majority of explorations have been focused on solids with square or tetragonal in-plane lattice structures such as Fe-based superconductors, characterized by Ising-like nematic order parameters. Unlike these systems, AV_3Sb_5 has a hexagonal in-plane lattice structure, in which rotational symmetry breaking states may be characterized by a three-state Potts model [9,48,51]. Previous pressure and strain studies have utilized similar nonlocal bulk techniques, predominantly focusing on studying the $2a_0 \times 2a_0$ CDW phase, and the competition between CDWs and superconductivity [20,52–64]. However, there is still little information related to if and how one can use strain to control smectic CDW domains, as well as if it is possible to rotate the director axis associated with the order. Understanding strain tunability, which reflects the underlying strength of electron-lattice coupling, holds important insights into the nature of this state.

Here, we study the impact of strain on the smectic CDWs in kagome superconductors CsV_3Sb_5 and KV_3Sb_5. We focus on the occasionally observed buckled regions of the sample and use a phase-sensitive analysis applied to atomically resolved STM topography to determine local in-plane strain. Our experiments reveal that the $4a_0$ charge-stripe order in CsV_3Sb_5 can be easily suppressed by strain. Moreover, we discover substantial deviations between the direction of the smectic electronic director of the $2a_0 \times 2a_0$ CDW and the direction of in-plane uniaxial strain, suggesting weak smectoelastic coupling in kagome superconductors. By studying different strained regions in more detail, we find that the misalignment of the electronic smectic director and anisotropic in-plane strain generally occurs in the regions with a large CDW gap. Our experiments provide an atomic-scale insight into the unusual interplay of strain and smectic orders in this family of materials, different from other commonly studied materials with a pronounced electronic directionality.

II. RESULTS

Bulk single crystals of AV_3Sb_5 cleave between hexagonal Sb layers and A layers [inset in Fig. 1(a), Sec. IV]. We focus on the Sb surface, which has a hexagonal morphology with in-plane lattice constants of $a \approx b \approx 5.5$ Å, consistent with diffraction measurements [34]. The V kagome layer, an essential ingredient in the crystal structure of these materials, resides just below the Sb surface imaged. Similarly to other experiments on CsV_3Sb_5 [21,30,38,65,66], typical STM topography of flat regions of the sample show both the $2a_0 \times 2a_0$ CDW modulations and the $4a_0$ charge-stripe order [Fig. 1(b)]. We proceed to explore how these smectic orders can be controlled by strain.

For this purpose, we focus on the occasionally encountered strained regions of the CsV_3Sb_5 sample. In Fig. 1(a), we show an area with a single bright "ripple" running across the field of view. By closely examining the topographic signal over this region and away from it, we find that the $4a_0$ charge-stripe order is markedly suppressed over the ripple [Figs. 1(d)–1(g), and Sec. I of Supplemental Material [67]]. This finding is supported by the FT of both the flat and the rippled region, where the $\mathbf{q}_{4a0}$ peak appears in the former [Figs. 1(b) and 1(c)] and disappears in the latter [Figs. 1(d) and 1(e), as well as Fig. 14 in Supplemental Material [67]]. Such buckled regions of the sample are generally induced by accidental strain [44,49,68]. To investigate this case quantitatively, we apply the Lawler-Fujita drift-correction algorithm [69] on the topography to extract the spatially varying strain tensor [49,50,69–72] (Sec. II of Supplemental Material [67]). From the x and y components of the displacement fields, $u_x(\boldsymbol{r})$ and $u_y(\boldsymbol{r})$, we can extract the strain tensor as

$$\boldsymbol{u}(\boldsymbol{r}) = \begin{pmatrix} u_{xx}(\boldsymbol{r}) & u_{xy}(\boldsymbol{r}) \\ u_{yx}(\boldsymbol{r}) & u_{yy}(\boldsymbol{r}) \end{pmatrix} = \begin{pmatrix} \partial_x u_x(\boldsymbol{r}) & \frac{1}{2}(\partial_y u_x(\boldsymbol{r}) + \partial_x u_y(\boldsymbol{r})) \\ \frac{1}{2}(\partial_y u_x(\boldsymbol{r}) + \partial_x u_y(\boldsymbol{r})) & \partial_y u_y(\boldsymbol{r}) \end{pmatrix},$$

where $u_{xx}(\boldsymbol{r})$ and $u_{yy}(\boldsymbol{r})$ are the strain map components along the x and y axes, and $u_{xy}(\boldsymbol{r}) = u_{yx}(\boldsymbol{r})$ are the shear strain components. Through basis transformation of the strain tensor matrix, we can extract strain components along any direction (Sec. III of Supplemental Material [67]). In particular, we can directly measure strain along $\boldsymbol{Q}^a_{\rm Bragg}$, $\boldsymbol{Q}^b_{\rm Bragg}$, and $\boldsymbol{Q}^c_{\rm Bragg}$ lattice directions independently, denoted as $u_{aa}(\boldsymbol{r})$, $u_{bb}(\boldsymbol{r})$, and $u_{cc}(\boldsymbol{r})$ [Figs. 1(h)–1(j)]. Positive values represent relative tensile strain, while negative values represent relative compressive strain. We note that these values are relative to the area away from the ripple, which we assume to be characterized by approximately zero strain. The most pronounced strain variation is observed along the $\boldsymbol{Q}^b_{\rm Bragg}$ and $\boldsymbol{Q}^c_{\rm Bragg}$ directions. By visual inspection of the $4a_0$ charge-stripe order intensity map [Fig. 1(g)] and in-plane strain components [Figs. 1(h)–1(j)], it is apparent that the $4a_0$ stripe order is suppressed near the topographic ripple where there is nonzero in-plane strain, which can have either positive or negative values in the strain maps. We calculate cross-correlation coefficients

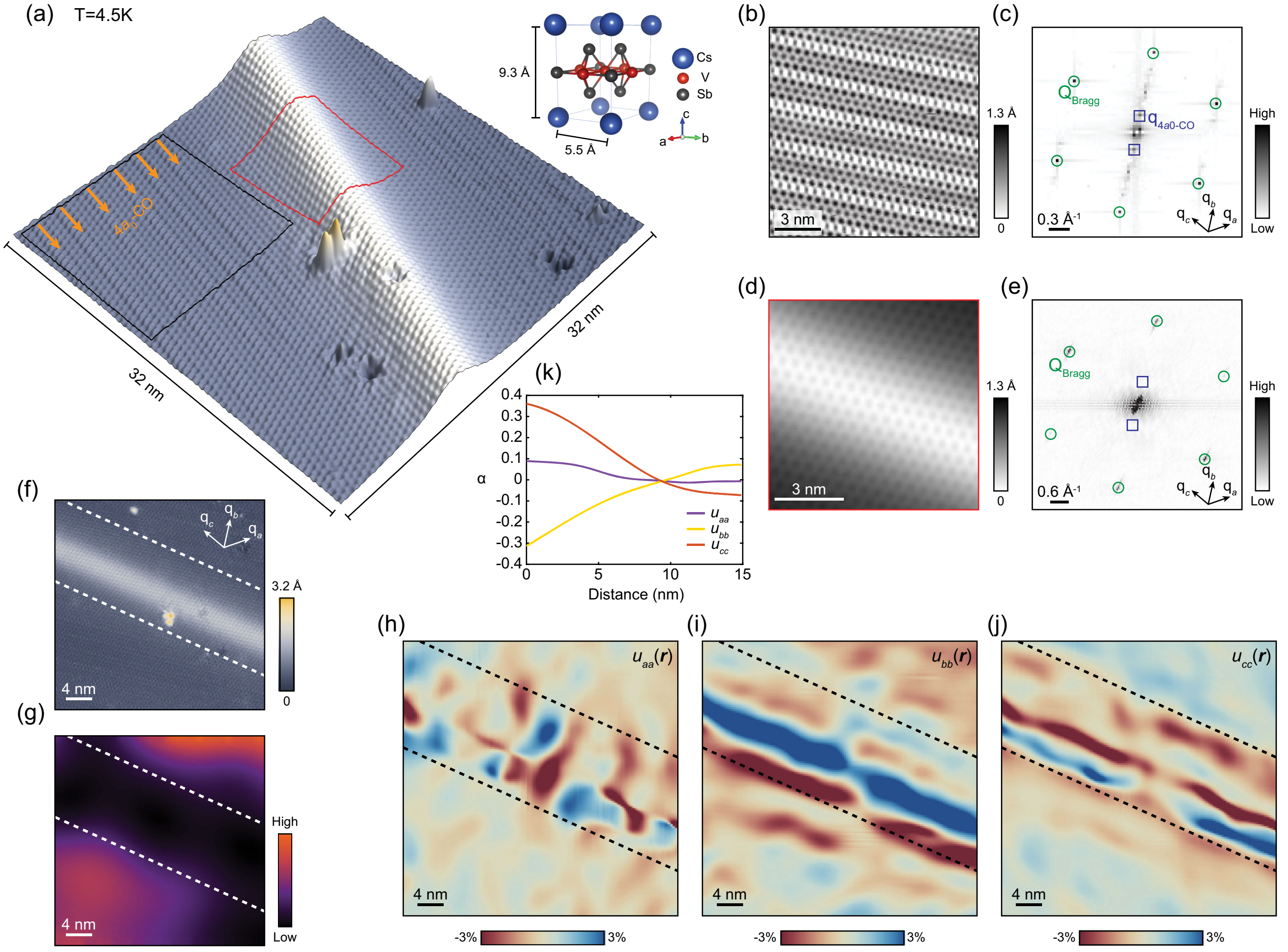

FIG. 1. Suppression of the $4a_0$ charge-stripe order under strain in CsV_3Sb_5. (a) A 3D portrayal of a 32-nm topography of a surface-corrugated region of the Sb termination. The orange arrows denote the $4a_0$ stripe order. The upper-right inset shows the crystal structure. (b) STM topography of the black square region in panel (a), with (c) its associated Fourier transform (FT), where Bragg peaks are circled in green and the $\mathbf{q}_{4a0}$ peak is enclosed in blue squares. (d) STM topography of the red square region in panel (a), and (e) the FT of panel (a) multiplied by a 1D Gaussian window function along the stripe, such that the image primarily contains the stripe area data, in which the $\mathbf{q}_{4a0}$ peak disappears. We note that the $2a_0$-by-$2a_0$ CDW peaks are difficult to discern in panel (e), but they are clearly visible in the Fourier transform of the entire region shown in panel (a) (Fig. 15 of Supplemental Material [67]). (f) STM topography of the same region as panel (a), with white dashed lines serving as a visual guide, marking the region without $4a_0$ stripe order. (g) The $4a_0$ stripe-order intensity map of panel (f), obtained from a larger 95-nm × 95-nm topography encompassing the area and cropped to match the exact area in panel (f). (h)–(j) Background subtracted strain maps of panel (f) along three reciprocal lattice directions $\boldsymbol{Q}^a_{\text{Bragg}}$, $\boldsymbol{Q}^b_{\text{Bragg}}$, and $\boldsymbol{Q}^c_{\text{Bragg}}$, respectively (Sec. II of Supplemental Material [67]). The black dashed lines denote the same non-$4a_0$ region in panels (f) and (g). Positive (negative) values indicate relative tensile (compressive) strain. (k) Radially averaged cross-correlation coefficients α between the $4a_0$ intensity map (g) and strain maps (h)–(j), plotted as a function of distance. The drift-correction length scale to extract the strain map is $3a_0$. The cross-correlation coefficient between two images $A(x,y)$ and $B(x,y)$ is defined as $\alpha(u,v) = \{[\sum_{x,y} A(x,y)B(x+u,y+v)]/[\sum_{x,y} A^2(x,y)\sum_{x,y} B^2(x+u,y+v)]\}$, where u and v are shifts along the x and y directions, respectively. Purple, yellow, and red curves represent the correlation along $\boldsymbol{Q}^a_{\text{Bragg}}$, $\boldsymbol{Q}^b_{\text{Bragg}}$, and $\boldsymbol{Q}^c_{\text{Bragg}}$, respectively. The error bar calculation of the cross-correlation coefficients is detailed in Fig. 16 of Supplemental Material [67]. The STM setup conditions are $V_{\text{sample}} = 40$ mV and $I_{\text{set}} = 100$ pA.

between the $4a_0$ charge-stripe order intensity map and different strain map components to a substantial cross-correlation for the $\boldsymbol{Q}^b_{\text{Bragg}}$ and $\boldsymbol{Q}^c_{\text{Bragg}}$ directions [Fig. 1(k), as well as Figs. 1 and 16 of Supplemental Material [67]]. From this calculation, it can be seen that the $4a_0$ order appears to be suppressed by strain that can be along different in-plane directions, both compressive (negative values) and tensile (positive values), which in part "washes out" the cross-correlations in Fig. 1(k). For instance, in Fig. 1(i), we can see that the $u_{bb}(\boldsymbol{r})$ map can be either positive or negative over the same region where the stripe order is suppressed.

We now turn to the impact of strain on the parent $2a_0 \times 2a_0$ CDW phase. Previous STM experiments thoroughly investigated the anisotropy of the CDW state to find that it is characterized by a dominant CDW direction different from the other two, which are approximately the same [5,6,24,38,65]. This finding suggests that rotation symmetry of the CDW state is reduced from C_6 to C_2 with a single remaining in-plane reflection symmetry along the dominant direction—a "smectic" CDW state. We define a smectic axis order parameter associated with the $2a_0 \times 2a_0$ CDW, equivalent to the nematic vector order parameter for the three-state Potts nematic state [9], which can be extracted locally from the intensities of the three CDW peaks $I^{a,b,c}_{2a_0}$ as $\boldsymbol{n} = (I^a_{2a_0} + I^c_{2a_0} - 2I^b_{2a_0}, \sqrt{3}(I^c_{2a_0} - I^a_{2a_0}))$. This process yields three main vector directions $\boldsymbol{n}$: $(1, -\sqrt{3})$, $(-2, 0)$, and $(1, \sqrt{3})$ corresponding to $\boldsymbol{q}^a_{2a_0}$,

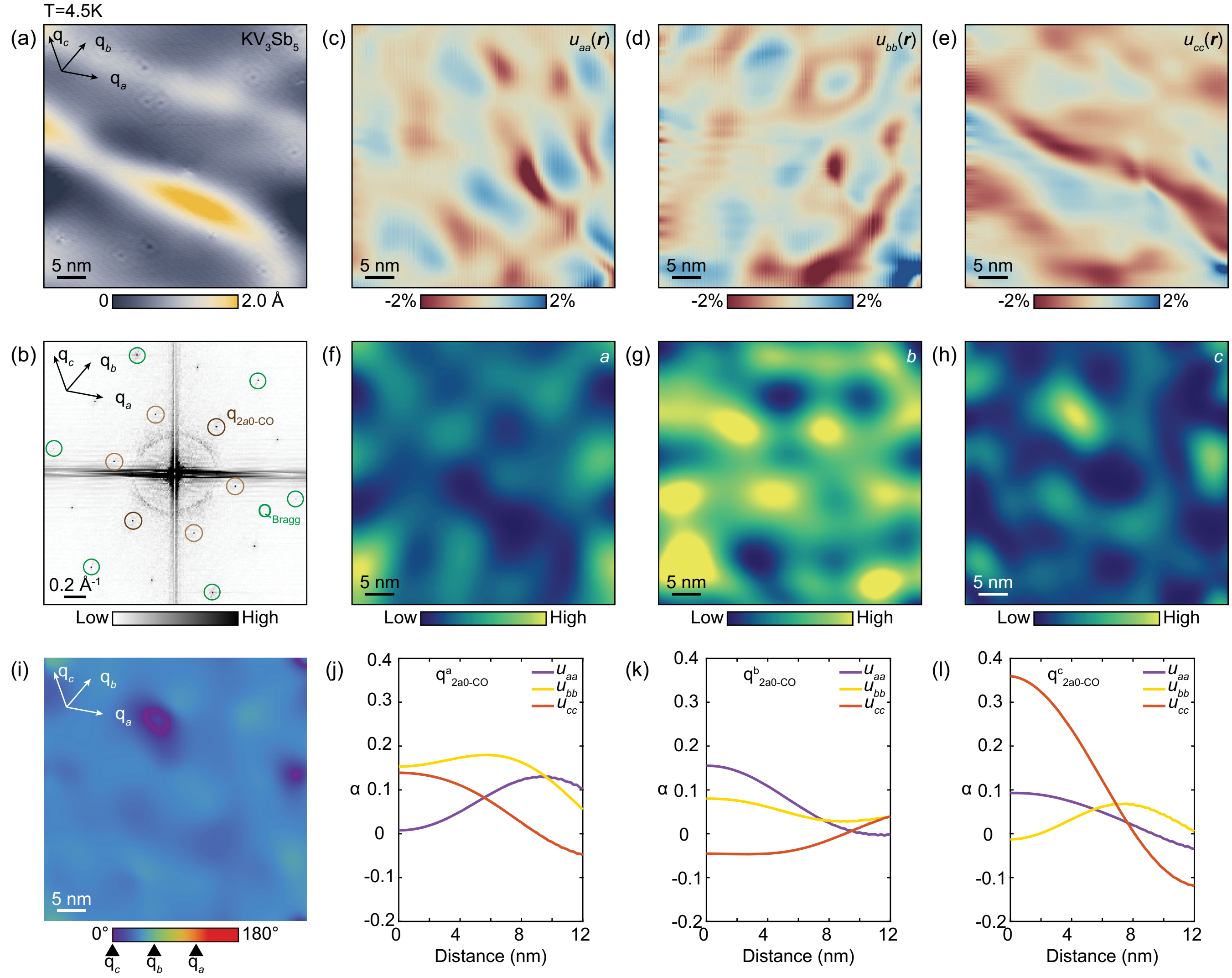

FIG. 2. Modulation of $2a_0$ CDW intensity under strain in KV_3Sb_5. (a), (b) STM topography of an Sb-terminated KV_3Sb_5 surface corrugated by strain and its FT. Green and brown circles indicate the atomic Bragg peaks and $\mathbf{q}_{2a0}$ peaks, respectively. (c)–(e) Strain maps over panel (a) along three reciprocal lattice directions after linear background subtraction to remove tip drift. The drift-correction length scale to extract the strain map is $3a_0$ (Sec. II of Supplemental Material [67]). (f)–(h) $2a_0$ CDW intensity maps along three reciprocal lattice directions, extracted from panel (a) and plotted in the same scale. (i) Angle map of the smectic vector order defined as $\boldsymbol{n}(\boldsymbol{r}) = (I^a_{2a_0}(\boldsymbol{r}) + I^c_{2a_0}(\boldsymbol{r}) - 2I^b_{2a_0}(\boldsymbol{r}), \sqrt{3}(I^c_{2a_0}(\boldsymbol{r}) - I^a_{2a_0}(\boldsymbol{r}))$, where $I^a_{2a_0}(\boldsymbol{r})$, $I^b_{2a_0}(\boldsymbol{r})$, and $I^c_{2a_0}(\boldsymbol{r})$ stand for the CDW intensity along $\boldsymbol{q}^a_{2a0}$, $\boldsymbol{q}^b_{2a0}$, and $\boldsymbol{q}^c_{2a0}$, respectively. The angle of each smectic vector $\boldsymbol{n}(\boldsymbol{r})$ is measured with respect to the $\boldsymbol{q}^b_{2a0}$ direction, and black triangles under the color bar denote the color representations of each reciprocal lattice direction. The average vector $\boldsymbol{n}(\boldsymbol{r})$ across the entire field is 47.0°, which is only 13.0° away from the $\boldsymbol{Q}^b_{\mathrm{Bragg}}$ direction. (j)–(l) Radially averaged cross-correlation coefficients between strain maps (c)–(e) and $2a_0$ CDW intensity maps (f)–(h), plotted as a function of distance. The color notation is the same as in Fig. 1(k). The STM setup conditions are $V_{\mathrm{sample}} = 100$ mV and $I_{\mathrm{set}} = 200$ pA.

$\boldsymbol{q}^{b}_{2a_0}$, and $\boldsymbol{q}^{c}_{2a_0}$, respectively (Sec. IV of Supplemental Material [67]).

We proceed to examine the simpler case of KV_3Sb_5, where the $4a_0$ stripe order is generally absent [Figs. 2(a) and 2(b)]. We analyze a region with strong spatial modulations and extract strain tensor components from the topography to map local strain [Figs. 2(c)–2(e)]. Strain appears to show the strongest variations along the $\boldsymbol{Q}^{c}_{\text{Bragg}}$ direction, with the spatial distribution qualitatively similar to those seen in the topography (Fig. 2 of Supplemental Material [67]). We create the intensity map of each $2a_0 \times 2a_0$ CDW peak $\boldsymbol{q}^{i}_{2a0}$ over the same region [Figs. 2(f)–2(h), as well as Sec. V of Supplemental Material [67]] and cross-correlate with the strain maps [Figs. 2(c)–2(e)]. The analysis shows a positive cross-correlation coefficient between the strain along $\boldsymbol{Q}^{c}_{\text{Bragg}}$ and the intensity of the $\boldsymbol{q}^{c}_{2a0}$ of about 0.35, sizable but still substantially lower than the perfect cross-correlation of 1 [Fig. 2(l)]. In other words, stretching the material along one lattice direction appears to lead to some concomitant change in the amplitude of the CDW peak along that same direction. It is worth noting that cross-correlation

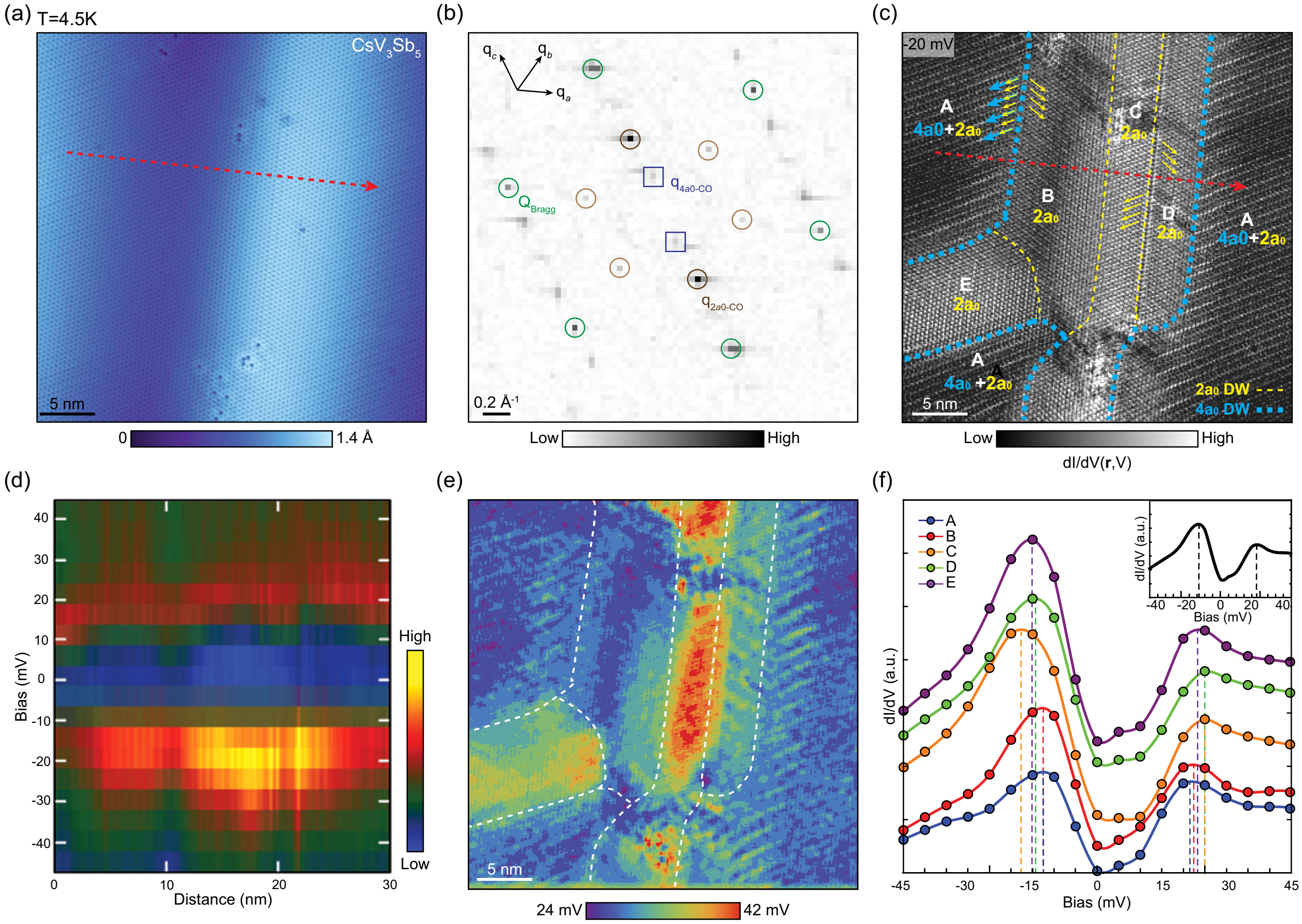

FIG. 3. Modulation of $2a_0$ CDW gap and rotation symmetry in CsV_3Sb_5. (a),(b) STM topography of Sb-terminated surface of CsV_3Sb_5 and its FT. Green circles, brown circles, and blue squares indicate the atomic Bragg peaks $\mathbf{q}_{2a0}$ and $\mathbf{q}_{4a0}$, respectively. (c) Representative $dI/dV(\boldsymbol{r}, V = -20\text{ mV})$ map of the same region as panel (a). Five domains A–E are determined by the wave-vector length and directions of the C_2 axis. Blue dashed lines are the domain wall between the $4a_0$ region and the non-$4a_0$ region. Yellow dashed lines are the domain wall between $2a_0$ CDW with a different C_2 axis. The blue arrows denote the local $4a_0$ stripe order directions, and yellow arrows denote the local $2a_0$ C_2 symmetric directions. (d) A 30-nm-long dI/dV spectra real-space linecut along the red dashed arrows in panels (a) and (c). (e) The $2a_0$ CDW gap map over the same region as panel (a). The gap size at each point $\boldsymbol{r}$ is determined by extracting the energy of local maxima for coherent peaks in dI/dV spectra near the Fermi level. (f) Spatially averaged dI/dV spectra (symbols) acquired over the five domains denoted by different colors. Solid curves connecting raw dI/dV points are obtained using polynomial function interpolation to connect discrete data points. The dashed lines mark the peak positions, signifying the gap size (Sec. VI of Supplemental Material [67]). Five curves are offset for clarity. The upper-right inset demonstrates the spatially averaged dI/dV spectra over the same region as panel (a). The STM setup conditions are $V_{\text{sample}} = 100$ mV, $V_{\text{exc}} = 5$ mV (rms), and $I_{\text{set}} = 300$ pA.

coefficients between strain along $\boldsymbol{Q}^b_{\mathrm{Bragg}}$ ($\boldsymbol{Q}^a_{\mathrm{Bragg}}$) directions and the intensity of the $\boldsymbol{q}^b_{2\mathrm{a}0}$ ($\boldsymbol{q}^a_{2\mathrm{a}0}$) are weak [Figs. 2(j) and 2(k)], which seemingly contradicts the finding. We hypothesize that the cross-correlation in these cases may be affected by the relatively featureless nature of strain maps along $\boldsymbol{Q}^c_{\mathrm{Bragg}}$ and $\boldsymbol{Q}^a_{\mathrm{Bragg}}$, with only a few localized strain "hotspots" that are not seen in corresponding CDW maps. This idea further highlights the lack of absolute control that strain has on controlling the $2a_0$ CDW intensities in this material. We hypothesize that these "hotspots" could be related to local strain caused by surface or subsurface impurities or vacancies, which may be interesting to explore in future work. Importantly, strain in this region does not alter the direction of the smectic director axis $\boldsymbol{n}$, which points approximately along $\boldsymbol{Q}^b_{\mathrm{Bragg}}$ in the whole field of view, despite in-plane strain of several percent stretching the lattice in the direction of $\boldsymbol{Q}^c_{\mathrm{Bragg}}$ [Fig. 2(i)].

To investigate this further, we examine an STM topography of $\mathrm{CsV_3Sb_5}$, where we find a more dramatic variation of electronic properties [Fig. 3(a)]. The FT of the STM

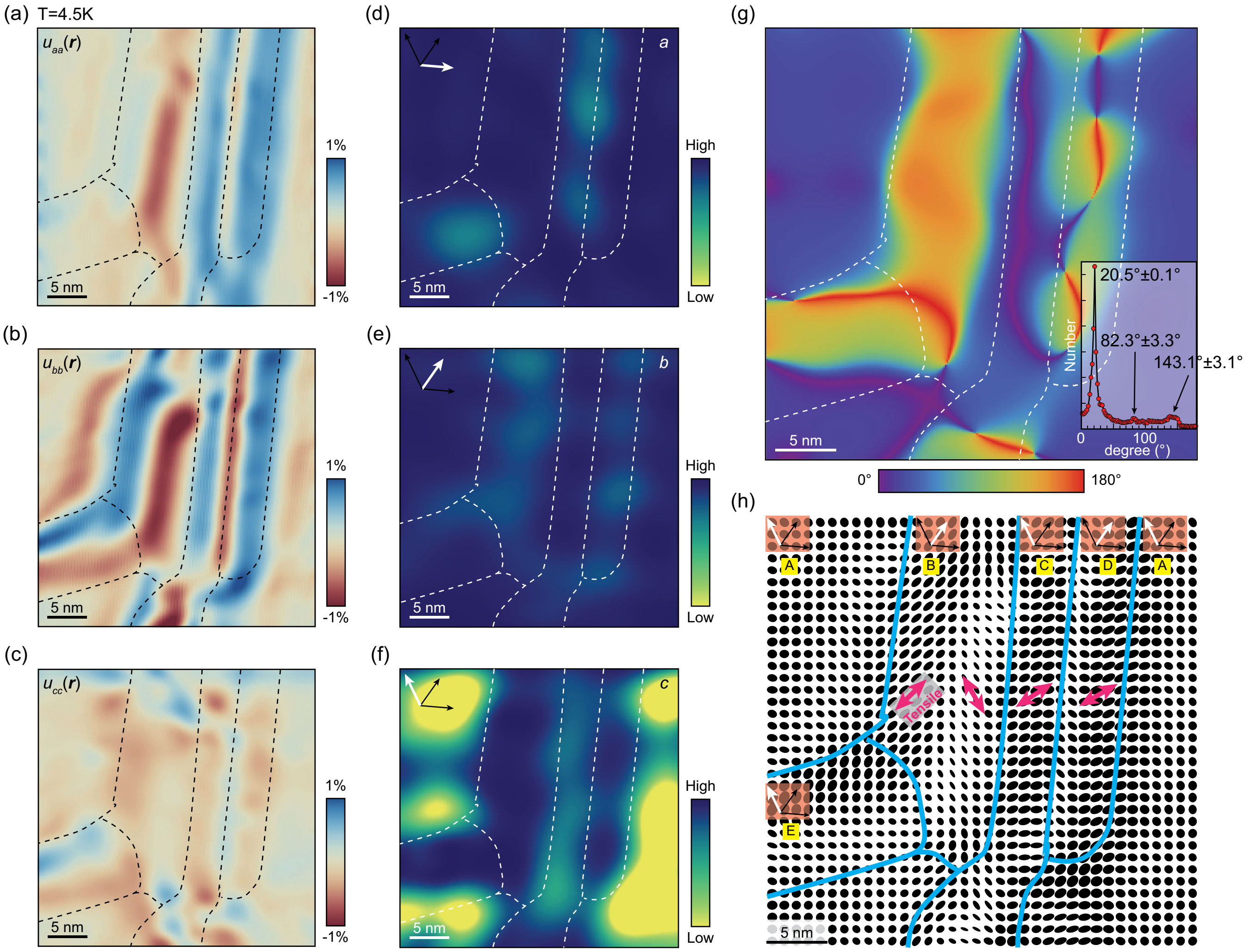

FIG. 4. Correlation between strain and rotation symmetry breaking in $\mathrm{CsV_3Sb_5}$. (a)–(c) Strain maps over Fig. 3(a) along three reciprocal lattice directions after quadratic background subtraction to remove tip drift. The drift-correction length scale to extract the strain map is $3\mathrm{a}_0$ (Sec. II of Supplemental Material [67]). Black dashed lines denote the domain boundary defined in Fig. 3(c). (d)–(f) Representative −20-mV CDW intensity maps along $\boldsymbol{q}^a_{2a0}$, $\boldsymbol{q}^b_{2a0}$, and $\boldsymbol{q}^c_{2a0}$, respectively. The white arrows in each subfigure denote the corresponding $2a_0$ CDW wave vector. (g) Smectic vector angle map over the same region, with the domain wall superimposed. The smectic order is defined as $\boldsymbol{n}(\boldsymbol{r}) = (I^a_{2a_0}(\boldsymbol{r}) + I^c_{2a_0}(\boldsymbol{r}) - 2I^b_{2a_0}(\boldsymbol{r}), \sqrt{3}(I^c_{2a_0}(\boldsymbol{r}) - I^a_{2a_0}(\boldsymbol{r}))$, the distribution of which is plotted in Fig. 9 of Supplemental Material [67]. The angle of each smectic vector is measured with respect to the (0, 1) direction. The lower-left histogram shows three dominant directions for the smectic vectors. (h) Map of lattice deformation, with blue lines denoting the CDW domain boundary. Isotropic disks represent the lattice without strain or with uniform strain; elliptical ones are unidirectionally stretched or compressed according to the main axis of ellipse. White arrows in each domain mark the dominant CDW direction. Pink arrows denote the local tensile strain directions. The STM setup condition are $V_{\mathrm{sample}} = 100$ mV, $V_{\mathrm{exc}} = 5$ mV (rms), and $I_{\mathrm{set}} = 300$ pA.

topography shows both the $\mathbf{q}_{2a0}$ and $\mathbf{q}_{4a0}$ wave vectors [Fig. 3(b)]. Similarly to what we discussed in Fig. 1, the $4a_0$ stripe order disappears in the middle region due to strain, and only the C_2 symmetric $2a_0$ CDW exists [Fig. 3(a), as well as Fig. 3 of Supplemental Material [67]], which provides us with a scenario of coexistence of only $2a_0$ CDW and strain in CsV_3Sb_5. Spatial variations of the smectic director axis can be determined by a visual inspection of a $dI/dV(\boldsymbol{r}, V = -20\text{ mV})$ map [Fig. 3(c)]. We pinpoint several distinct regions, labeled in alphabetical order from A to E, outlined by dashed lines across which the smectic director axis rotates towards a different Bragg peak direction. The identification of the rotation axis for each domain is further supported by the CDW amplitude profiles (Fig. 4 of Supplemental Material [67]).

Another insight comes from measuring the spectral gap variations. The gap at the Fermi level measured in the average dI/dV spectrum is about 35 meV, which agrees with the magnitude of the $2a_0 \times 2a_0$ CDW gap reported in previous STM work [4,5,21,30]. This local CDW gap, however, varies in different regions. A linecut of dI/dV spectra acquired across individual regions A, B, C, and D illustrates the gap size modulation [Fig. 3(d), as well as Figs. 5 and 6 of Supplemental Material [67]]. From this linecut, we can further exclude the idea that the dominant spectral gap arises from the $4a_0$ charge-stripe order, as nearly identical gap edges are observed in regions A and B, with and without the $4a_0$ stripe order. By mapping the gap size for each pixel in the field of view, we create a gap map [Fig. 3(e), as well as Sec. VI and Fig. 7 of Supplemental Material [67]], which shows tantalizing similarities to the smectic domain morphology. Domain C contains the largest CDW gap, whereas domain A exhibits the smallest ones [Fig. 3(f)].

Similar to the procedure used in Figs. 1 and 2, we extract in-plane strain maps $u_{aa}(\boldsymbol{r})$, $u_{bb}(\boldsymbol{r})$, and $u_{cc}(\boldsymbol{r})$ from the STM topography in Fig. 3(a) [Figs. 4(a)–4(c), as well as Fig. 8 of Supplemental Material [67]]. To visualize if the area is locally deformed isotropically or anisotropically, we plot a real-space lattice deformation map based on the full strain tensor $\boldsymbol{u}(\boldsymbol{r})$ [Fig. 4(h), as well as Sec. VII of Supplemental Material [67]]. In this map, isotropic disks represent either isotropic or zero strain, while elongated ellipses denote tensile strain that is parallel to the major axis of the ellipse. The relative variation of the area for each disk reflects the change of the in-plane unit cell area. In general, the more deformed the disk is, the more pronounced the corresponding in-plane strain is. To accompany local strain mapping, we extract three CDW intensity maps [Figs. 4(d)–4(f), as well as Sec. V of Supplemental Material [67]] and plot the angle $\theta(\boldsymbol{n}(\boldsymbol{r}))$ of the smectic director $\boldsymbol{n}(\boldsymbol{r})$ with respect to the y axis [Fig. 4(g), as well as Fig. 9 of Supplemental Material [67]] over the identical region of the sample to visualize smectic domains [Fig. 4(h), as well as Fig. 10 of Supplemental Material [67]]. This domain-wall distribution remains nearly constant through different energies close to the Fermi level (Fig. 11 of Supplemental Material [67]), which is consistent with energy-independent $2a_0$ CDW rotation symmetry. In the $\theta(\boldsymbol{n})$ map, there are three different majority vectors at $20.5° \pm 0.1°$, $82.3° \pm 3.3°$, and $143.1° \pm 3.1°$, which correspond to the three possible directions of the smectic order parameter. This method provides a more quantitative measurement of smectic domains, which are generally consistent with the domain walls picked out by visual inspection of data in Fig. 3(c).

Laying domain walls over the deformation map reveals important insights. Domain A away from the rippled area [upper-left and lower-right corners of Fig. 4(h)] exhibits the $4a_0$ charge-stripe order consistently seen on the nominally unstrained surfaces of CsV_3Sb_5, suggesting minimal strain. None of the other regions in the field of view show the $4a_0$ charge order. Domain B shows two types of relative anisotropic strain—stretching along $\boldsymbol{Q}^b_{\text{Bragg}}$ relative to the perpendicular direction (left part) and compression primarily along $\boldsymbol{Q}^b_{\text{Bragg}}$ relative to the perpendicular direction (right part)—but maintains the $\boldsymbol{q}^b_{2a0}$ smectic axis throughout. Notably, domain C shows the electronic smectic axis along $\boldsymbol{q}^c_{2a0}$ despite tensile strain along $\boldsymbol{Q}^b_{\text{Bragg}}$. On the other hand, smectic director in domain D is the same as the direction of tensile strain. Overall, our data in Figs. 2 and 4 demonstrate that the C_2 smectic CDW director axis can rotate in response to uniaxial strain in only some of the nanoscale regions.

III. DISCUSSION

To shed light on this intriguing observation, we turn to the variation of spectral gaps between different regions. In particular, we can observe that regions where C_2 electronic smectic director axis and uniaxial strain are misaligned generally show a larger CDW gap, for example, domain C and the right half of domain B. In analogy to the definition of nematic susceptibility, we can define smectic susceptibility $\chi_{\text{smec}} = [(\partial\bar{n})/(\partial u)]$ ($\bar{n}$ is the average smectic vector) in a three-state Potts model. We can write the Hamiltonian for the system as $H = -\sum_{\langle i,j\rangle} J_{ij} n_i n_j - \sum_i u_i n_i$, where n_i is the site-dependent smectic vector, J_{ij} is the site-dependent coupling constant, and u_i is the site-dependent magnitude of tensile strain. When χ_{smec} is large, it is energetically costly to misalign the smectic vector and the strain field; however, when χ_{smec} is small, the energy loss of the misalignment between the local smectic vector and the strain field can be compensated by the gain in the coupling energy of neighboring smectic vectors themselves. Thus, we can see that the critical strain required to switch the C_2 axis to be along a different direction is relatively large, which makes it a “hard” C_2 smectic electronic axis (with small χ_{smec}), analogous to a hard magnet that resists the saturation of the magnetization in the magnetic field.

Our STM experiments shed light on the relationship between smectic CDWs and strain in kagome superconductors. We find that strain can induce a complete suppression of the $4a_0$ charge-stripe order in CsV_3Sb_5 while the $2a_0 \times 2a_0$ CDW remains present. The fact that strain leads to the disappearance of the $4a_0$ charge-stripe order before the $2a_0 \times 2a_0$ CDW is also consistent with the smaller onset temperature of the $4a_0$ charge order compared to that of the $2a_0 \times 2a_0$ CDW [30]. At this point, it is difficult to conclusively disentangle the roles of in-plane vs out-of-plane strain in the suppression of the $4a_0$ order, but it is conceivable that both play a role. Although we cannot measure it exactly in our experiments, out-of-plane strain is likely to be the strongest in the narrow region along the topographic ripple where apparent topographic buckling is the most pronounced.

Interestingly, the spontaneously formed C_2 smectic director axis of the $2a_0 \times 2a_0$ CDW generally does not follow the direction of uniaxial strain (Sec. VIII and Fig. 13 of Supplemental Material [67]). In principle, the smectic vector could choose one of the three degenerate states most closely aligned with the direction of the tensile strain to minimize the total energy. We hypothesize that stronger electron correlation driving the larger CDW gap in turn substantially reduces smectic susceptibility so that the in-plane uniaxial strain field fails to rotate the overall smectic vector. This variation of the CDW gap can, in part, be attributed to the modulations in the out-of-plane strain, i.e., interlayer distance, as revealed by bulk-sensitive strain measurements [20,64,73], where the CDW gap increases when interlayer distance increases.

It is interesting to compare our observations to the extensive elastotransport experiments studying the coupling of electrons and the approximately square lattice in the nematic phase of Fe-based superconductors [42,47,50]. While two types of "twin" electronic nematic domains are routinely observed in bulk single crystals, these can be easily detwined by small amounts of uniaxial strain of less than 1% [42,74–76]. In contrast, in AV_3Sb_5, it appears that substantially larger strain does not consistently align the smectic director axis, which could be an important insight for elastotransport measurements on these systems. STM experiments on bulk single crystals of the Fe-based superconductor Fe(Te,Se) using similar strain methodology found that electronic nematicity aligns and is enhanced by antisymmetric strain, but there is no decoupling between the two [49]. It is interesting to note that in severely strained molecular-beam-epitaxy-grown FeSe thin films with an intentionally induced dense network of edge dislocations, electronic nematicity generally follows strain direction, except in tiny regions where the two are decoupled [50]. In contrast to the strain-induced smectic phase in non-nematic LiFeAs [77], our work reveals an opposite scenario in AV_3Sb_5—the smectic order forms spontaneously, and the smectic director diverges from the strain direction substantially, as opposed to aligning predictably. Locally strained regions in AV_3Sb_5 provide a fortuitous platform to study the effects of strain using a local probe to test the stiffness of smectic CDWs. This platform could serve as a useful methodology to provide fresh insights into the control of electronic directionality in other correlated materials.

IV. METHODS

Single crystals of CsV_3Sb_5 and KV_3Sb_5 were grown and characterized as described in more detail in Refs. [32,34]. We cold cleaved the crystals at low temperature as described in Ref. [30] and quickly inserted them into the STM head. STM data were acquired using a customized Unisoku USM1300 microscope at approximately 4.5 K. Spectroscopic measurements were made using a standard lock-in technique with 910-Hz frequency and bias excitation as also detailed in the figure captions. STM tips used were homemade, chemically etched tungsten tips, annealed in UHV to bright orange color prior to STM experiments.

ACKNOWLEDGMENTS

I. Z. gratefully acknowledges the support from the National Science Foundation (NSF), Division of Materials Research 2216080. B. R. O. acknowledges the support from U.S. Department of Energy (DOE), Office of Science, Basic Energy Sciences (BES), Materials Sciences and Engineering Division. S. D. W, B. R. O, and A. C. S. acknowledge support via the UC Santa Barbara NSF Quantum Foundry funded via the Q-AMASE-i program under award DMR-1906325. Z. W. is supported by the U.S. Department of Energy, Basic Energy Sciences Grant No. DE-FG02-99ER45747 and by the Cottrell SEED Award No. 27856 from Research Corporation for Science Advancement. We are thankful to Zhenyu Wang, Rafael Fernandes and Jiun-Haw Chu for valuable feedback and discussions. We also thank Zhuying Wang for the careful reading of the manuscript.

H. L., S. C., and H. Z. performed the STM experiments. Y. W. analyzed the data under the guidance of H. L. and I. Z. B. R. O. and A. C. S. synthesized and characterized the samples under the supervision of S. D. W. Z. W. provided theoretical input on the interpretation of STM data. H. L, Y. W., S. D. W., Z. W., and I. Z. wrote the paper with input from all the authors. I. Z. supervised the project.

The authors declare no competing interests.

DATA AVAILABILITY

Experimental data supporting the conclusions can be obtained from the corresponding author upon reasonable request.

[1] E. Fradkin, S. A. Kivelson, and J. M. Tranquada, *Colloquium: Theory of intertwined orders in high temperature superconductors*, Rev. Mod. Phys. **87**, 457 (2015).

[2] R. M. Fernandes, A. V. Chubukov, and J. Schmalian, *What drives nematic order in iron-based superconductors?*, Nat. Phys. **10**, 97 (2014).

[3] C. Rubio-Verdú *et al.*, *Moiré nematic phase in twisted double bilayer grapheme*, Nat. Phys. **18**, 196 (2022).

[4] Y.-X. Jiang *et al.*, *Unconventional chiral charge order in kagome superconductor* $\mathrm{KV_3Sb_5}$, Nat. Mater. **20**, 1353 (2021).

[5] H. Li *et al.*, *Rotation symmetry breaking in the normal state of a kagome superconductor* $\mathrm{KV_3Sb_5}$, Nat. Phys. **18**, 265 (2022).

[6] Y. Xu *et al.*, *Three-state nematicity and magneto-optical Kerr effect in the charge density waves in kagome superconductors*, Nat. Phys. **18**, 1470 (2022).

[7] Y. Xiang *et al.*, *Twofold symmetry of c-axis resistivity in topological kagome superconductor* $\mathrm{CsV_3Sb_5}$ *with in-plane rotating magnetic field*, Nat. Commun. **12**, 6727 (2021).

[8] Q. Wu *et al.*, *Simultaneous formation of two-fold rotation symmetry with charge order in the kagome superconductor* $\mathrm{CsV_3Sb_5}$ *by optical polarization rotation measurement*, Phys. Rev. B **106**, 205109 (2022).

[9] M. H. Christensen, T. Birol, B. M. Andersen, and R. M. Fernandes, *Theory of the charge density wave in* $\mathrm{AV_3Sb_5}$ *kagome metals*, Phys. Rev. B **104**, 214513 (2021).

[10] H. Tan, Y. Liu, Z. Wang, and B. Yan, *Charge density waves and electronic properties of superconducting kagome metals*, Phys. Rev. Lett. **127**, 046401 (2021).

[11] M. M. Denner, R. Thomale, and T. Neupert, *Analysis of charge order in the kagome metal* $\mathrm{AV_3Sb_5}$ *(*$\mathrm{A = K, Rb, Cs}$*)*, Phys. Rev. Lett. **127**, 217601 (2021).

[12] J. Frassineti *et al.*, *Microscopic nature of the charge-density wave in the kagome superconductor* $\mathrm{RbV_3Sb_5}$, Phys. Rev. Res. **5**, L012017 (2023).

[13] H. Li, X. Liu, Y. B. Kim, and H.-Y. Kee, *Origin of* π*-shifted three-dimensional charge density waves in the kagomé metal* $\mathrm{AV_3Sb_5}$ *(*$\mathrm{A = Cs,\ Rb,\ K}$*)*, Phys. Rev. B **108**, 075102 (2023).

[14] F. Grandi, A. Consiglio, M. A. Sentef, R. Thomale, and D. M. Kennes, *Theory of nematic charge orders in kagome metals*, Phys. Rev. B **107**, 155131 (2023).

[15] L. Kautzsch *et al.*, *Incommensurate charge-stripe correlations in the kagome superconductor* $\mathrm{CsV_3Sb_{5-x}Sn_x}$, npj Quantum Mater. **8**, 37 (2023).

[16] Y.-P. Lin and R. M. Nandkishore, *Complex charge density waves at van Hove singularity on hexagonal lattices: Haldane-model phase diagram and potential realization in the kagome metals* $\mathrm{AV_3Sb_5}$ *(*$\mathrm{A = K, Rb, Cs}$*)*, Phys. Rev. B **104**, 045122 (2021).

[17] R. Khasanov *et al.*, *Time-reversal symmetry broken by charge order in* $\mathrm{CsV_3Sb_5}$, Phys. Rev. Res. **4**, 023244 (2022).

[18] C. Farhang, J. Wang, B. R. Ortiz, S. D. Wilson, and J. Xia, *Unconventional specular optical rotation in the charge ordered state of kagome metal* $\mathrm{CsV_3Sb_5}$, Nat. Commun. **14**, 5326 (2023).

[19] H. Li *et al.*, *Discovery of conjoined charge density waves in the kagome superconductor* $\mathrm{CsV_3Sb_5}$, Nat. Commun. **13**, 6348 (2022).

[20] T. Qian *et al.*, *Revealing the competition between charge density wave and superconductivity in* $\mathrm{CsV_3Sb_5}$ *through uniaxial strain*, Phys. Rev. B **104**, 144506 (2021).

[21] Z. Liang *et al.*, *Three-dimensional charge density wave and surface-dependent vortex-core states in a kagome superconductor* $\mathrm{CsV_3Sb_5}$, Phys. Rev. X **11**, 031026 (2021).

[22] C. Mielke III *et al.*, *Time-reversal symmetry-breaking charge order in a kagome superconductor*, Nature (London) **602**, 245 (2022).

[23] T. Park, M. Ye, and L. Balents, *Electronic instabilities of kagome metals: Saddle points and Landau theory*, Phys. Rev. B **104**, 035142 (2021).

[24] L. Nie *et al.*, *Charge-density-wave-driven electronic nematicity in a kagome superconductor*, Nature (London) **604**, 59 (2022).

[25] N. Ratcliff, L. Hallett, B. R. Ortiz, S. D. Wilson, and J. W. Harter, *Coherent phonon spectroscopy and interlayer modulation of charge density wave order in the kagome metal* $\mathrm{CsV_3Sb_5}$, Phys. Rev. Mater. **5**, L111801 (2021).

[26] C. Candelora *et al.*, *Quantifying magnetic field driven lattice distortions in kagome metals at the femto-scale using scanning tunneling microscopy*, Phys. Rev. B **109**, 155121 (2024).

[27] H.-S. Xu *et al.*, *Multiband superconductivity with sign-preserving order parameter in kagome superconductor* $\mathrm{CsV_3Sb_5}$, Phys. Rev. Lett. **127**, 187004 (2021).

[28] C. Guo *et al.*, *Switchable chiral transport in charge-ordered kagome metal* $\mathrm{CsV_3Sb_5}$, Nature (London) **611**, 461 (2022).

[29] H. Li *et al.*, *No observation of chiral flux current in the topological kagome metal* $\mathrm{CsV_3Sb_5}$, Phys. Rev. B **105**, 045102 (2022).

[30] H. Zhao, *Cascade of correlated electron states in the kagome superconductor* $\mathrm{CsV_3Sb_5}$, Nature (London) **599**, 216 (2021).

[31] H. Li, *Small Fermi pockets intertwined with charge stripes, and pair density wave order in a kagome superconductor*, Phys. Rev. X **13**, 031030 (2023).

[32] B. R. Ortiz *et al.*, $\mathrm{CsV_3Sb_5}$*: A* $\mathrm{Z_2}$ *topological kagome metal with a superconducting ground state*, Phys. Rev. Lett. **125**, 247002 (2020).

[33] H. Li *et al.*, *Observation of unconventional charge density wave without acoustic phonon anomaly in kagome superconductors* $\mathrm{AV_3Sb_5}$ *(*$\mathrm{A = Rb, Cs}$*)*, Phys. Rev. X **11**, 031050 (2021).

[34] B. R. Ortiz *et al.*, *Superconductivity in the* $\mathrm{Z_2}$ *kagome metal* $\mathrm{KV_3Sb_5}$, Phys. Rev. Mater. **5**, 034801 (2021).

[35] X. Feng, K. Jiang, Z. Wang, and J. Hu, *Chiral flux phase in the kagome superconductor* $\mathrm{AV_3Sb_5}$, Sci. Bull. **66**, 1384 (2021).

[36] M. H. Christensen, T. Birol, B. M. Andersen, and R. M. Fernandes, *Loop currents in* $\mathrm{AV_3Sb_5}$ *kagome metals: Multipolar and toroidal magnetic orders*, Phys. Rev. B **106**, 144504 (2022).

[37] S. Zhou and Z. Wang, *Chern Fermi pocket, topological pair density wave, and charge-4e and charge-6e superconductivity in kagomé superconductors*, Nat. Commun. **13**, 7288 (2022).

[38] H. Li *et al.*, *Unidirectional coherent quasiparticles in the high-temperature rotational symmetry broken phase of*

AV_3Sb_5 *kagome superconductors*, Nat. Phys. **19**, 637 (2023).

[39] S. A. Kivelson, E. Fradkin, and V. J. Emery, *Electronic liquid-crystal phases of a doped Mott insulator*, Nature (London) **393**, 550 (1998).

[40] S. D. Wilson and B. R. Ortiz, AV_3Sb_5 *kagome superconductors*, Nat. Rev. Mater. **9**, 420 (2024) .

[41] T. Worasaran *et al.*, *Nematic quantum criticality in an Fe-based superconductor revealed by strain-tuning*, Science **372**, 973 (2021).

[42] J.-H. Chu *et al.*, *In-plane resistivity anisotropy in an underdoped iron arsenide superconductor*, Science **329**, 824 (2010).

[43] I. Kostylev, S. Yonezawa, Z. Wang, Y. Ando, and Y. Maeno, *Uniaxial-strain control of nematic superconductivity in* $Sr_xBi_2Se_3$, Nat. Commun. **11**, 4152 (2020).

[44] A. Soumyanarayanan *et al.*, *Quantum phase transition from triangular to stripe charge order in* $NbSe_2$, Proc. Natl. Acad. Sci. U.S.A. **110**, 1623 (2013).

[45] S. Gao *et al.*, *Atomic-scale strain manipulation of a charge density wave*, Proc. Natl. Acad. Sci. U.S.A. **115**, 6986 (2018).

[46] F. Cossu, K. Palotás, S. Sarkar, I. Di Marco, and A. Akbari, *Strain-induced stripe phase in charge-ordered single layer* $NbSe_2$, NPG Asia Mater. **12**, 24 (2020).

[47] J.-H. Chu, H.-H. Kuo, J. G. Analytis, and I. R. Fisher, *Divergent nematic susceptibility in an iron arsenide superconductor*, Science **337**, 710 (2012).

[48] A. R. Chakraborty and R. M. Fernandes, *Strain-tuned quantum criticality in electronic Potts-nematic systems*, Phys. Rev. B **107**, 195136 (2023).

[49] H. Zhao, *Nematic transition and nanoscale suppression of superconductivity in* Fe(Te, Se), Nat. Phys. **17**, 903 (2021).

[50] Z. Ren *et al.*, *Nanoscale decoupling of electronic nematicity and structural anisotropy in* FeSe *thin films*, Nat. Commun. **12**, 10 (2021).

[51] R. M. Fernandes and J. W. F. Venderbos, *Nematicity with a twist: Rotational symmetry breaking in a moiré superlattice*, Sci. Adv. **6**, eaba8834 (2020).

[52] F. H. Yu *et al.*, *Unusual competition of superconductivity and charge-density-wave state in a compressed topological kagome metal*, Nat. Commun. **12**, 3645 (2021).

[53] N. N. Wang *et al.*, *Competition between charge-density-wave and superconductivity in the kagome metal* RbV_3Sb_5, Phys. Rev. Res. **3**, 043018 (2021).

[54] K. Y. Chen *et al.*, *Double superconducting dome and triple enhancement of* T_c *in the kagome superconductor* CsV_3Sb_5 *under high pressure*, Phys. Rev. Lett. **126**, 247001 (2021).

[55] H. LaBollita and A. S. Botana, *Tuning the van Hove singularities in* AV_3Sb_5 $(A = K, Rb, Cs)$ *via pressure and doping*, Phys. Rev. B **104**, 205129 (2021).

[56] L. Yin *et al.*, *Strain-sensitive superconductivity in the kagome metals* KV_3Sb_5 *and* CsV_3Sb_5 *probed by point-contact spectroscopy*, Phys. Rev. B **104**, 174507 (2021).

[57] F. Du *et al.*, *Pressure-induced double superconducting domes and charge instability in the kagome metal* KV_3Sb_5, Phys. Rev. B **103**, L220504 (2021).

[58] Z. Zhang *et al.*, *Pressure-induced reemergence of superconductivity in the topological kagome metal* CsV_3Sb_5, Phys. Rev. B **103**, 224513 (2021).

[59] A. Consiglio *et al.*, *Van Hove tuning of* AV_3Sb_5 *kagome metals under pressure and strain*, Phys. Rev. B **105**, 165146 (2022).

[60] F. Yu *et al.*, *Pressure-induced dimensional crossover in a kagome superconductor*, Phys. Rev. Lett. **128**, 077001 (2022).

[61] F. Du *et al.*, *Superconductivity modulated by structural phase transitions in pressurized vanadium-based kagome metals*, Phys. Rev. B **106**, 024516 (2022).

[62] F. Du *et al.*, *Evolution of superconductivity and charge order in pressurized* RbV_3Sb_5, Chin. Phys. B **31**, 017404 (2022).

[63] C. C. Zhu *et al.*, *Double-dome superconductivity under pressure in the V-based kagome metals* AV_3Sb_5 $(A = \mathrm{Rb\ and\ K})$, Phys. Rev. B **105**, 094507 (2022).

[64] Z. Liu *et al.*, *Absence of nematic instability in the kagome metal* CsV_3Sb_5, Phys. Rev. X **14**, 031015 (2024).

[65] P. Wu *et al.*, *Unidirectional electron–phonon coupling in the nematic state of a kagome superconductor*, Nat. Phys. **19**, 1143 (2023).

[66] H. Chen *et al.*, *Roton pair density wave in a strong-coupling kagome superconductor*, Nature (London) **599**, 222 (2021).

[67] See Supplemental Material at http://link.aps.org/supplemental/10.1103/PhysRevX.15.021074 for a detailed description of analysis methods: drift correction, strain and CDW intensity extraction, smectic order parameter definition and the simulation.

[68] L. Cao *et al.*, *Two distinct superconducting states controlled by orientations of local wrinkles in* LiFeAs, Nat. Commun. **12**, 6312 (2021).

[69] M. J. Lawler *et al.*, *Intra-unit-cell electronic nematicity of the high-*T_c *copper-oxide pseudogap states*, Nature (London) **466**, 347 (2010).

[70] D. Walkup *et al.*, *Interplay of orbital effects and nanoscale strain in topological crystalline insulators*, Nat. Commun. **9**, 1550 (2018).

[71] S. Sharma, H. Li, Z. Ren, W. A. Castro, and I. Zeljkovic, *Nanoscale visualization of the thermally driven evolution of antiferromagnetic domains in* FeTe *thin films*, Phys. Rev. Mater. **7**, 074401 (2023).

[72] Z. Ren, H. Li, H. Zhao, S. Sharma, and I. Zeljkovic, *Rotation of the dislocation grid in multilayer* FeSe *films and visualization of electronic nematic domains via orbital-selective tunneling*, Phys. Rev. Mater. **6**, 124802 (2022).

[73] M. Frachet *et al.*, *Colossal c-axis response and lack of rotational symmetry breaking within the kagome plane of the* CsV_3Sb_5 *superconductor*, Phys. Rev. Lett. **132**, 186001 (2024).

[74] T. Chen, M. Yi, and P. Dai, *Electronic and magnetic anisotropies in* FeSe *family of iron-based superconductors*, Front. Phys. **8**, 314 (2020).

[75] J. Schmidt *et al.*, *Nematicity in the superconducting mixed state of strain detwinned underdoped* $Ba(Fe_{1-x}Co_x)_2As_2$, Phys. Rev. B **99**, 064515 (2019).

[76] M. A. Tanatar *et al.*, *Origin of the resistivity anisotropy in the nematic phase of* FeSe, Phys. Rev. Lett. **117**, 127001 (2016).

[77] C. M. Yim, *Discovery of a strain-stabilised smectic electronic order in* LiFeAs, Nat. Commun. **9**, 2602 (2018).